Analytical Model for Magnetic-Geared Double-Rotor Machines and Its d-q Axis Determination

Hang Zhao, Chunhua Liu, Zaixin Song, Senyi Liu, Thierry Lubin

Analytical Model for Magnetic-Geared Double-Rotor Machines and Its *d-q* Axis Determination

Hang Zhao [1, 2], Chunhua Liu [1, 2]*, Zaixin Song [1, 2], Senyi Liu [1, 2], and Thierry Lubin [3]
[1] School of Energy and Environment, City University of Hong Kong, Kowloon Tong, Hong Kong
[2] Shenzhen Research Institute, City University of Hong Kong, Nanshan District, Shenzhen 518057, China
[3] Groupe de Recherche en Énergie Electrique de Nancy (GREEN), Faculté des Sciences et Technologies, Université de Lorraine, 54506 Vandœuvre-lès-Nancy, France.
*Corresponding author: Chunhua Liu; chunliu@cityu.edu.hk

Abstract: This paper presents an analytical subdomain model for the prediction of various electromagnetic parameters of magnetic-geared double-rotor machine (MGDRM). By dividing the MGDRM into six subdomains and solving the Maxwell equations in polar coordinates for each region, the vector magnetic potential distribution can be derived. Subsequently, the flux density distribution, back electromotive force (EMF), and output torque, can be calculated. Furthermore, based on the proposed model, the equivalent *d-q* axis is elaborated. Also, the corresponding *d* and *q* inductance can be obtained. It proves that the MGDRM can be regarded as a non-salient-pole synchronous machine. Besides, the power factor of the MGDRM under i_d=0 control is deduced and optimized for the different thicknesses of modulators. In addition, the demagnetization capability is analysed by adopting the subdomain model. Finally, the accuracy of proposed subdomain model for MGDRMs is validated via the finite-element method (FEM).

Nomenclature

A_z	Vector magnetic potential.
B_r, B_θ	Radial and tangential component of magnetic flux density.
$\vec{M}$, $\vec{J}$	Magnetization vector of magnets, Current density vector.
μ_0	Magnetic permeability of vacuum.
P, Q	Number of stator slots and modulator pieces.
P_i	Pole pair Number of inner rotor permanent magnets (PMs).
β, γ, δ	Modulator opening angle, stator slot width angle and slot opening angle.
φ_0, θ_0	Initial circumferential position of the inner rotor and modulator.
θ_i, θ_j, J_l	Circumferential positions of PMs, i^{th} modulator opening and j^{th} slot opening, current density in the l^{th} slot.
R_1, R_2, R_3, R_4	Radii of inner rotor yoke, inner rotor outer surface, modulator inner surface, modulator outer surface.
R_5, R_6, R_7	Radii of stator bore, slot top, slot bottom.
L	Axial length of the machine.
D	Root mean square (RMS) current density in windings.
B_r, B'_r	PM remanence at normal temperature and at 120 °C.
N, K, T, M	Harmonic order used in air gap and PM subdomain, modulator subdomain, slot opening subdomain and slot subdomain.
φ_l, ψ, ψ_d, ψ_q	Flux linkages of one coil side, certain phase, *d* axis and *q* axis.
L_{xx}, M_{xy}	Self inductance of phase x, mutual inductance between phase x and y.
L_d, L_q	Inductance of *d* axis and *q* axis.
E, f	Back electromagnetic force (EMF) and current frequency of windings.
α, φ	Electric angle of the equivalent d axis, power factor angle of the machine.
Ω_{in}, Ω_{out}, Ω_d	Rotating speed of inner rotor, modulator and equivalent *d* axis.
T_{rot}, T_{mod}	Electromagnetic torque of inner rotor and modulator.

1. Introduction

Due to the high efficiency, long range and smooth start, hybrid electric vehicles (HEVs) are taking up the more share in the whole vehicle market [1]. One of the key components in HEV is the power split device (PSD), which allows the internal combustion engine (ICE) and the electric motor to provide the drive power at different ratios [2]. The existing PSDs in HEVs, such as Toyota Prius and Honda Insight, have adopted the gearbox to realize the power distribution, which inevitably decreases the efficiency and introduces the vibration and noise.

The magnetic-geared double-rotor machine (MGDRM) has a great potential for serving as the PSD in HEVs [3], [4], since it utilizes the electromagnetic force to transmit the power among different moving components. Thus, it can eliminate the disadvantages caused by the physical contact in mechanical gearboxes. The operating principle and structure requirements, such as the pole pair combination and winding configuration of MGDRMs, are investigated in [5]. Also, a step-skew modulator structure is introduced to solve the asymmetrical flux path problem, whose cogging torque can be significantly reduced [6]. In addition, the AlNiCo material and magnetizing windings are adopted to realize the gear-ratio variation in [7]. Besides, to enhance the flux-weakening ability of MGDRM, a consequent-pole and inserted PM structure are discussed in [8]. Moreover, PMs are inserted into the gap of modulator to increase the torque density or interact with extra windings in [9], [10].

Particularly, an accurate expression of the air-gap magnetic field distribution of MGDRMs is necessary to evaluate the performance and executing optimization at the initial design stage. The finite element method (FEM) can assist the designers to obtain the magnetic field distribution within a machine with the high accuracy. However, the mesh density of FEM should be high enough to acquire the electromagnetic parameters as accurately as possible, which further increases the computation time. Nevertheless, the numerical result in each mesh can be obtained, which would blurry the understanding of the fundamental principle of a certain machine. This is exactly true for MGDRMs, since it utilizes the magnetic-gearing effect. The magnetic field distribution is complex with the introduction of modulator [11].

Another approach of machine design is the magnetic equivalent circuits (MECs), which have been developed for decades [12], [13]. However, the nodes in MEC must be selected delicately to reflect the flux paths within the machine. The motion of rotor makes the modeling even complicated [14]. Since MGDRMs have two rotating components, MEC is unsuitable for the design and optimization. Besides, the analytical model based on conformal transformation is very useful in predicting the air-gap magnetic flux distribution by taking into account of the slotting effect [15-17]. This method cannot be applied in analyzing the magnetic field of MGDRMs, because the modulation poles on the modulator cannot be regarded as equipotential.

The third approach of machine design is the subdomain model, which is an effective analytical method for solving the magnetic field of various electromagnetic devices. By dividing the machine into several subdomain regions, solving Maxwell equations within each region, and applying Fourier series to satisfy the boundary conditions, the magnetic field distribution can be achieved [18], [19]. In fact, various machine topologies have been investigated by using the subdomain model method [20-25]. In fact, the calculation time of FEM increases immensely with the size of electric machine. Yet, the calculation time of subdomain model is only related to the number of harmonic orders for a given electric machine. Therefore, the subdomain model could offer the convenience to engineers at the initial stage of motor design.

Although the analytical model of magnetic-geared machines with the single outer rotor is given in [26], the procedure of derivation is not given in detail. In particular, the rotation of modulator is not discussed. To the authors' knowledge, the comprehensive characteristics, operating principle and performances of MGDRMs have not been well investigated with an accurate analytical model in previous studies.

This paper proposes a subdomain model for MGDRMs, which can effectively predict the magnetic field distribution and secondary parameters in high accuracy. First, the modeling process of MGDRM is developed in Section II. Then, the calculated magnetic field distribution, back EMF, and torque-angle relation are verified by FEM. In addition, the equivalent *d-q* axis of MGDRM is initially acquired by using the subdomain model, and i_d=0 control is applied to get the maximal output torque. Moreover, the power factor and demagnetization capability of MGDRM are also analyzed.

2. Subdomain Model

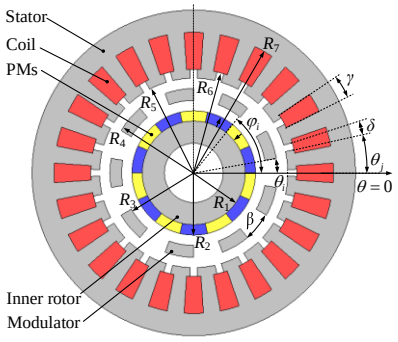

Fig. 1. *Geometry of the investigated MGDRM*

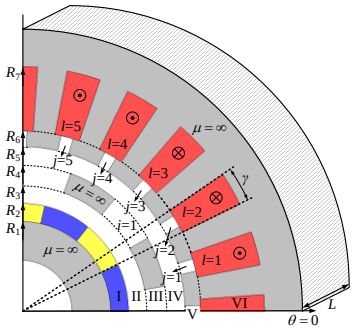

Fig. 2. *The symbol and definitions of subdomains*

A fourteen-pole/twenty-four-slot MGDRM with nine ferromagnetic bars and single-layer winding is investigated in this paper to verify the proposed method. It should be noted that the proposed model is also suitable for double-layer-winding machine by changing the expression of current density in each slot. Since there are currents flowing through the windings, vector magnetic potential is adopted to calculate the magnetic field distribution within the MGDRM. The geometry of the investigated MGDRM is shown in Fig.1: the modulator is composed of equally distributed iron bars on circumferential direction, serving as the outer rotor of the MGDRM. φ_0, θ_0 are the initial circumferential position of the inner rotor and modulator, respectively, they are defined as zero where the positions of inner rotor and modulator are as shown in Fig.1. θ_i, θ_j can be further given by:

$$\theta_i = -\frac{\beta}{2} + \frac{2i\pi}{Q} + \theta_0 \quad \text{with } 1 \le i \le Q \tag{1}$$

$$\theta_j = -\frac{\delta}{2} + \frac{2j\pi}{Q} \quad \text{with } 1 \le j \le P \tag{2}$$

Assumptions are made to simplify the calculation as:

(1) The magnetic field on the axial direction is regarded as zero, and the end effect is ignored [27];

(2) The permeability of soft-magnetic material is assumed to be infinite. Thus, the magnetic field strength direction should be vertical to the soft-magnetic boundary, namely it does not have tangential direction value. Also, the magnetic field strength is zero within the iron;

(3) The relative permeability of permanent magnets (PMs) and coil is assumed to be 1;

(4) The geometrical structure side of MGDRM is parallel to either θ or r direction in polar coordinates.

As shown in Fig. 2, the MGDRM can be divided into several subdomains: PM (Region I), inner air gap (Region II), modulator opening (Region III), outer air gap (Region IV), slot opening (Region V) and stator slot (Region VI). The connections among different subdomains can be expressed as boundary conditions. The magnetostatic Maxwell equation is satisfied in each subdomain, which can be further reduced to Poisson's equation or Laplace's equations under aforementioned assumptions. Then, by utilizing the method of separation of variables in polar coordinates, the general expression of vector magnetic potential in each subdomain can be obtained. Finally, the Fourier coefficients within these expressions can be achieved by solving the boundary condition equations. To simplify the equation form, the following notations are adopted in this paper:

$$P_z(x,y)=\left(\frac{x}{y}\right)^z+\left(\frac{y}{x}\right)^z \quad \text{and} \quad E_z(x,y)=\left(\frac{x}{y}\right)^z-\left(\frac{y}{x}\right)^z \tag{3}$$

2.1. Boundary Condition

In polar coordinates, the flux density can be decomposed into the radial and tangential component B_r, B_θ. Their relations with the vector magnetic potential are as:

$$B_r=\frac{1}{r}\frac{\partial A}{\partial \theta} \quad \text{and} \quad B_\theta=-\frac{\partial A}{\partial r} \tag{4}$$

For simplification, the following boundary conditions are all expressed by using the vector magnetic potential.

Actually, the boundary conditions are inserted at the boundaries of different regions, which can be divided into three forms for the proposed MGDRM.

(1) Periodic condition: In tangential direction, the magnetic field distribution has a period of 2π, thus:

$$A_i(r,\theta)=A_j(r,\theta+2\pi) \tag{5}$$

(2) Continuous condition: The vector magnetic potential should be continuous at the interface between two regions:

$$\begin{cases} A_i(r,\Theta)=A_j(r,\Theta) & \text{Boundary is radial, } \Theta \text{ is a constant} \\ A_i(R,\theta)=A_j(R,\theta) & \text{Boundary is tangential, } R \text{ is a constant} \end{cases} \tag{6}$$

(3) Neumann condition: Generally, the tangential component of the magnetic field intensity $\boldsymbol{H}$ should be continuous at the interface. Therefore, air region and coil region have:

$$\begin{cases} \left.\frac{\partial A_i}{\partial \theta}\right|_{\theta=\Theta}=\left.\frac{\partial A_j}{\partial \theta}\right|_{\theta=\Theta} & \text{Boundary is in radial direction} \\ \left.\frac{\partial A_i}{\partial r}\right|_{r=R}=\left.\frac{\partial A_j}{\partial r}\right|_{r=R} & \text{Boundary is in tangential direction} \end{cases} \tag{7}$$

Table 1 Boundary Conditions of Each Subdomain

Regions	Boundary condition		Applied range	Regions	Boundary condition		Applied range
I	$\left.\frac{\partial A_I}{\partial r}\right\|_{r=R_1}=0$	(8)	$\theta\in[0,2\pi]$	IV, V	$\left.\frac{\partial A_{IV}}{\partial r}\right\|_{r=R_5}=h(\theta)=\begin{cases}\left.\frac{\partial A_j}{\partial r}\right\|_{r=R_5}\\ 0\end{cases}$	(9)	$\begin{cases}\theta\in[\theta_j,\theta_j+\delta]\\ elsewhere\end{cases}$
I, II	$A_I(R_2,\theta)=A_{II}(R_2,\theta)$	(10)	$\theta\in[0,2\pi]$	IV, V	$A_j(R_5,\theta)=A_{IV}(R_5,\theta)$	(11)	$\theta\in[0,2\pi]$
I, II	$\left.\frac{\partial A_{II}}{\partial r}\right\|_{r=R_2}=\left.\frac{\partial A_I}{\partial r}\right\|_{r=R_2}$	(12)	$\theta\in[0,2\pi]$	V	$\begin{cases}\left.\frac{\partial A_j}{\partial \theta}\right\|_{\theta=\theta_j}=0\\ \left.\frac{\partial A_j}{\partial \theta}\right\|_{\theta=\theta_j+\delta}=0\end{cases}$	(13)	$r\in[R_5,R_6]$
II, III	$\left.\frac{\partial A_{II}}{\partial r}\right\|_{r=R_3}=f(\theta)=\begin{cases}\left.\frac{\partial A_i}{\partial r}\right\|_{r=R_3}\\ 0\end{cases}$	(14)	$\begin{cases}\theta\in[\theta_i,\theta_i+\beta]\\ elsewhere\end{cases}$	V, VI	$A_j(R_6,\theta)=A_i(R_6,\theta)$	(15)	$\theta\in[0,2\pi]$
II, III	$A_i(R_3,\theta)=A_{II}(R_3,\theta)$	(16)	$\theta\in[0,2\pi]$	V, VI	$\left.\frac{\partial A_i}{\partial r}\right\|_{r=R_6}=s(\theta)=\begin{cases}\left.\frac{\partial A_j}{\partial r}\right\|_{r=R_6}\\ 0\end{cases}$	(17)	$\begin{cases}\theta\in[\theta_j,\theta_j+\delta]\\ elsewhere\end{cases}$
III	$\begin{cases}\left.\frac{\partial A_i}{\partial \theta}\right\|_{\theta=\theta_i}=0\\ \left.\frac{\partial A_i}{\partial \theta}\right\|_{\theta=\theta_i+\beta}=0\end{cases}$	(18)	$r\in[R_2,R_3]$	VI	$\begin{cases}\left.\frac{\partial A_i}{\partial \theta}\right\|_{\theta=\theta_j+\frac{1}{2}(\delta-\gamma)}=0\\ \left.\frac{\partial A_i}{\partial \theta}\right\|_{\theta=\theta_j+\frac{1}{2}(\delta+\gamma)}=0\end{cases}\ (l=j)$	(19)	$r\in[R_6,R_7]$
III, IV	$A_i(R_4,\theta)=A_{IV}(R_4,\theta)$	(20)	$\theta\in[0,2\pi]$				
III, IV	$\left.\frac{\partial A_{IV}}{\partial r}\right\|_{r=R_4}=g(\theta)=\begin{cases}\left.\frac{\partial A_i}{\partial r}\right\|_{r=R_4}\\ 0\end{cases}$	(22)	$\begin{cases}\theta\in[\theta_i,\theta_i+\beta]\\ elsewhere\end{cases}$	VI	$\left.\frac{\partial A_i}{\partial r}\right\|_{r=R_7}=0$	(21)	$\theta\in[\theta_j+\frac{1}{2}(\delta-\gamma),\ \theta_j+\frac{1}{2}(\delta+\gamma)]$

Since $\boldsymbol{H}$=0 within the soft-magnetic material, then the boundary condition for the interface with soft-magnetic material can be expressed as:

$$\begin{cases} \left.\dfrac{\partial A_i}{\partial \theta}\right|_{\theta=\Theta} = 0 & \text{Boundary is in radial direction} \\ \left.\dfrac{\partial A_i}{\partial r}\right|_{r=R} = 0 & \text{Boundary is in tangential direction} \end{cases} \tag{23}$$

By adopting the different boundary condition forms in the different regions of MGDRM, Table 1 can be obtained.

Besides, from [28], the Region III and Region V have Neumann boundary conditions. Extra constraints should be exerted to guarantee the existence of solution [29].

$$\sum_{i=1}^{Q} B_0^i = 0 \quad \text{and} \quad \sum_{j=1}^{P} B_0^j = 0 \tag{24}$$

By using (68) to replace B_0^j with J_l, one can get:

$$\sum_{l=1}^{P} J_l = 0 \tag{25}$$

where (25) can be satisfied automatically, if the windings are energized with three-phase symmetrical currents.

2.2. General Solution of Poisson's and Laplace's Equations

Generally, if Coulomb gauge is adopted, the vector magnetic potential for every region should satisfy:

$$\nabla^2 A = -\mu_0(\nabla \times \vec{M}) - \mu_0 \vec{J} \tag{26}$$

In regions where $\vec{M}$ and $\vec{J}$ are zero, (26) is reduced to Laplace's equation:

$$\nabla^2 A = 0 \tag{27}$$

Thus, the vector magnetic potential in different regions should follow:

$$\nabla^2 A = 0 \quad \text{in region II, III, IV, V} \tag{28}$$

$$\nabla^2 A = -\mu_0(\nabla \times \vec{M}) \quad \text{in region I} \tag{29}$$

$$\nabla^2 A = -\mu_0 \vec{J} \quad \text{in region VI} \tag{30}$$

Under polar coordinate, (28), (29), (30) can be written as:

$$\frac{\partial A_i}{\partial r^2} + \frac{1}{r}\frac{\partial A_i}{\partial r} + \frac{1}{r^2}\frac{\partial A_i}{\partial \theta^2} = 0 \quad \text{with } i\text{=II, III, IV, V} \tag{31}$$

$$\frac{\partial A_I}{\partial r^2} + \frac{1}{r}\frac{\partial A_I}{\partial r} + \frac{1}{r^2}\frac{\partial A_I}{\partial \theta^2} = \frac{\mu_0}{r}\frac{\partial M}{\partial \theta} \tag{32}$$

$$\frac{\partial A_j}{\partial r^2} + \frac{1}{r}\frac{\partial A_j}{\partial r} + \frac{1}{r^2}\frac{\partial A_j}{\partial \theta^2} = -\mu_0 J_j \quad \text{with } 1 \le j \le P \tag{33}$$

By taking into account the boundary conditions in Table 1, the expressions of vector magnetic potential can be obtained, as shown in Table 2. Besides, the detailed Fourier coefficients are given in Appendix.

Finally, by solving the system of first-order linear equation, the Fourier coefficients of each expression can be obtained. So, the exact expression of vector magnetic potential in each subdomain is acquired.

2.3. Flux Density and Torque Calculation

By utilizing (39) and (4), the radial and tangential components of flux density in outer air gap can be derived as:

$$\begin{aligned} B_{IVr}(r,\theta) = &-\sum_{n=1}^{\infty}\Big(A_n^{IV}\frac{R_4}{r}\frac{P_n(r,R_5)}{E_n(R_4,R_5)} \\ &+ B_n^{IV}\frac{R_5}{r}\frac{P_n(r,R_4)}{E_n(R_5,R_4)}\Big)\sin(n\theta) \\ &+\sum_{n=1}^{\infty}\Big(C_n^{IV}\frac{R_4}{r}\frac{P_n(r,R_5)}{E_n(R_4,R_5)} + D_n^{IV}\frac{R_5}{r}\frac{P_n(r,R_4)}{E_n(R_5,R_4)}\Big)\cos(n\theta) \end{aligned} \tag{34}$$

$$\begin{aligned} B_{IV\theta}(r,\theta) = &-\sum_{n=1}^{\infty}\Big(A_n^{IV}\frac{R_4}{r}\frac{E_n(r,R_5)}{E_n(R_4,R_5)} \\ &+ B_n^{IV}\frac{R_5}{r}\frac{E_n(r,R_4)}{E_n(R_5,R_4)}\Big)\cos(n\theta) \\ &-\sum_{n=1}^{\infty}\Big(C_n^{IV}\frac{R_4}{r}\frac{E_n(r,R_5)}{E_n(R_4,R_5)} + D_n^{IV}\frac{R_5}{r}\frac{E_n(r,R_4)}{E_n(R_5,R_4)}\Big)\sin(n\theta) \end{aligned} \tag{35}$$

Table 2 Expressions of Vector Magnetic Potentials in Each Subdomain

Regions	Corresponding vector potential expression
I	$A_I(r,\theta) = A_0^I + \sum_{n=1}^{\infty}\Big(A_n^I\frac{P_n(r,R_1)}{P_n(R_2,R_1)} + X_n(r)\cos(n\varphi_i)\Big)\cos(n\theta) + \sum_{n=1}^{\infty}\Big(C_n^I\frac{P_n(r,R_1)}{P_n(R_2,R_1)} + X_n(r)\sin(n\varphi_i)\Big)\sin(n\theta)$ (36)
II	$A_{II}(r,\theta) = A_0^{II} + \sum_{n=1}^{\infty}\Big(A_n^{II}\frac{R_2}{n}\frac{P_n(r,R_3)}{E_n(R_2,R_3)} + B_n^{II}\frac{R_3}{n}\frac{P_n(r,R_2)}{E_n(R_3,R_2)}\Big)\cos(n\theta) + \sum_{n=1}^{\infty}\Big(C_n^{II}\frac{R_2}{n}\frac{P_n(r,R_3)}{E_n(R_2,R_3)} + D_n^{II}\frac{R_3}{n}\frac{P_n(r,R_2)}{E_n(R_3,R_2)}\Big)\sin(n\theta)$ (37)
III	$A_i(r,\theta) = A_0^i + B_0^i\ln r + \sum_{k=1}^{\infty}\Big(A_k^i\frac{E_{k\pi/\beta}(r,R_4)}{E_{k\pi/\beta}(R_3,R_4)} - B_k^i\frac{E_{k\pi/\beta}(r,R_3)}{E_{k\pi/\beta}(R_3,R_4)}\Big)\cos\Big(\frac{k\pi}{\beta}(\theta-\theta_i)\Big)$ (38)
IV	$A_{IV}(r,\theta) = A_0^{IV} + \sum_{n=1}^{\infty}\Big(A_n^{IV}\frac{R_4}{n}\frac{P_n(r,R_5)}{E_n(R_4,R_5)} + B_n^{IV}\frac{R_5}{n}\frac{P_n(r,R_4)}{E_n(R_5,R_4)}\Big)\cos(n\theta) + \sum_{n=1}^{\infty}\Big(C_n^{IV}\frac{R_4}{n}\frac{P_n(r,R_5)}{E_n(R_4,R_5)} + D_n^{IV}\frac{R_5}{n}\frac{P_n(r,R_4)}{E_n(R_5,R_4)}\Big)\sin(n\theta)$ (39)
V	$A_j(r,\theta) = A_0^j + B_0^j\ln r + \sum_{t=1}^{\infty}\Big(A_t^i\frac{E_{t\pi/\delta}(r,R_6)}{E_{t\pi/\delta}(R_5,R_6)} - B_t^i\frac{E_{t\pi/\delta}(r,R_5)}{E_{t\pi/\delta}(R_5,R_6)}\Big)\cos\Big(\frac{t\pi}{\delta}(\theta-\theta_j)\Big)$ (40)
VI	$A_l(r,\theta) = A_0^l + \frac{1}{2}\mu_0 J_l(R_7^2\ln r - \frac{1}{2}r^2) + \sum_{m=1}^{\infty}A_m^l\frac{\gamma R_6}{m\pi}\frac{P_{m\pi/\gamma}(r,R_7)}{E_{m\pi/\gamma}(R_6,R_7)}\cos\Big(\frac{m\pi}{\gamma}(\theta-\theta_j-\frac{1}{2}(\delta-\gamma))\Big)$ (41)

Similarly, the expression of radial, tangential component of flux density $B_{IIr}(r,\theta)$, $B_{II\theta}(r,\theta)$ can be calculated by replacing R_4, R_5 with R_2 and R_3, and A_n^{II}, B_n^{II}, C_n^{II}, D_n^{II} with A_n^{IV}, B_n^{IV}, C_n^{IV}, D_n^{IV} in (34) and (35) [28].

According to the Maxwell stress tensor expression, the electromagnetic torque of inner air gap T_{ein} and outer air gap T_{eout} can be expressed as:

$$T_{ein} = \frac{LR_i^2}{\mu_0}\int_0^{2\pi} B_{IIr}(R_i,\theta)B_{II\theta}(R_i,\theta)d\theta \tag{42}$$

$$T_{eout} = \frac{LR_o^2}{\mu_0}\int_0^{2\pi} B_{IVr}(R_o,\theta)B_{IV\theta}(R_o,\theta)d\theta \tag{43}$$

where R_{i}, R_{o} are the average radii of inner air gap and outer air gap, respectively. R_{i}, R_{o} are given by:

$$R_i = \frac{R_2+R_3}{2}, \quad R_o = \frac{R_4+R_5}{2} \tag{44}$$

For the inner rotor, only T_{ein} is exerted to drive it. However, the modulator is driven by T_{ein} and T_{eout} simultaneously. Hence, the resultant electromagnetic torque on the inner rotor T_{rot} and modulator T_{mod} can be expressed as:

$$T_{rot} = T_{ein}, \quad T_{mod} = T_{eout} - T_{ein} \tag{45}$$

2.4. Flux Linkage and Back EMF Calculation

The flux linkage of each coil can be calculated as:

$$\phi_l = L\frac{N_{turn}}{A_{slot}}\int_{R_6}^{R_7}\int_{\theta_j+\frac{1}{2}(\delta-\gamma)}^{\theta_j+\frac{1}{2}(\delta+\gamma)} A_l r d\theta dr \tag{46}$$

where A_{slot} is the cross-sectional area of each slot as given by:

$$A_{slot} = \frac{\delta}{2}(R_7^2 - R_6^2) \tag{47}$$

The coil connection of each phase is given by a matrix as:

$$C_0 = \begin{bmatrix} 1 & 0 & 0 & 0 & 0 & -1 & -1 & 0 & 0 & 0 & 0 & 1 \\ 0 & 0 & 0 & 1 & 1 & 0 & 0 & 0 & 0 & -1 & -1 & 0 \\ 0 & -1 & -1 & 0 & 0 & 0 & 0 & 1 & 1 & 0 & 0 & 0 \\ 1 & 0 & 0 & 0 & 0 & -1 & -1 & 0 & 0 & 0 & 0 & 1 \\ 0 & 0 & 0 & 1 & 1 & 0 & 0 & 0 & 0 & -1 & -1 & 0 \\ 0 & -1 & -1 & 0 & 0 & 0 & 0 & 1 & 1 & 0 & 0 & 0 \end{bmatrix} \tag{48}$$

Therefore, the flux linkage of each phase can be derived by:

$$\boldsymbol{\psi} = \begin{bmatrix} \psi_A \\ \psi_B \\ \psi_C \end{bmatrix} = C\left[\phi_1, \phi_2, \ldots \phi_l, \ldots \phi_{24}\right]^T \tag{49}$$

The three-phase back EMF can be calculated as:

$$\begin{bmatrix} E_A \\ E_B \\ E_C \end{bmatrix} = -\frac{d\psi}{dt} = \frac{\psi\big|_{\varphi_i+\omega_{in}\Delta t,\theta_i+\omega_{out}\Delta t} - \psi\big|_{\varphi_i,\theta_i}}{\Delta t} \tag{50}$$

3. Analytical Prediction and FEM Validation

To validate the effectiveness of the proposed subdomain model, the analytical prediction is compared with the 2-D FEM result and considered the saturation effect of soft-magnetic material from the tool of JMAG Designer. Table 3 gives the parameters of the investigated 14-pole/24-slot MGDRM. The FEM model has 80952 elements, 50581 nodes; the element size near the air gap is set as 0.5 mm to maintain the calculation accuracy. The calculation time of one step by FEM is 16.98 s, while it only takes 7.65 s to run a single step by the subdomain model. So, the proposed method could help designers to save the time at primary stage of motor design.

Table 3 Geometrical Parameters of MGDRM

Symbol	Value	Symbol	Value
R_1	40 mm	P_{i}	7
R_2	50 mm	P	24
R_3	52 mm	Q	9
R_4	62 mm	B_{r}	1.21 T
R_5	64 mm	B_r'	1.08 T
R_6	66 mm	D	5 A/mm^2
R_7	95 mm	N	100
L	110 mm	K	100
β	π/9 rad	T	100
δ	π/60 rad	M	100
γ	π/24 rad	-	-

Figures 3-7 show the comparisons between the analytical prediction and FEM calculation results, where φ_0=0, θ_0=0. Figure 3 and 4 show the no-load the radial and tangential flux density distribution for inner air gap and outer air gap; Figure 5 and 6 show the radial and tangential flux density distribution for inner air gap and outer air gap when the windings are electrified with AC current. It can be seen that the outer air-gap flux density distribution changes greatly after the windings are electrified, while that of inner air gap changes slightly. Figure 7 shows the back-EMF under no-load condition， where the rotating speed of inner rotor and modulator are 600 r/min and 400/3 r/min, respectively. A good agreement between the analytical prediction given by the subdomain model and FEM simulation can be seen for all these figures. However, due to the magnetic saturation within the modulator pieces and slot teeth of MGDRM, a small difference of magnetic flux density can still be observed, as shown in Fig. 4 and Fig. 6. Besides, the magnetic saturation becomes severe as the current increases in the stator windings, since the magnetic flux density difference is larger in Fig. 6 compared to that in Fig. 4.

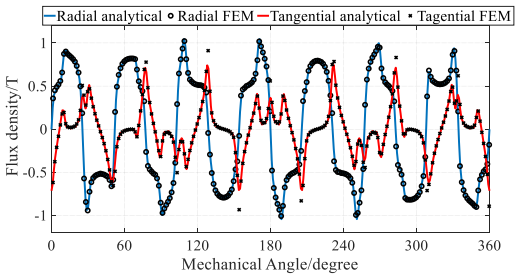

Fig. 3. *Analytically predicted and FEM calculated results with no-load inner air-gap flux density distribution*

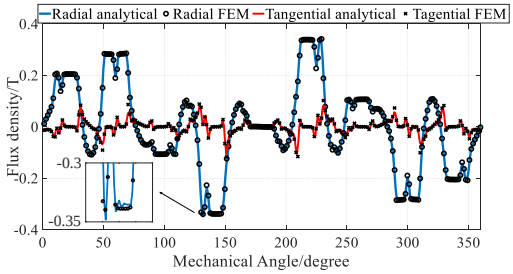

Fig. 4. Analytically predicted and FEM calculated results with no-load outer air-gap flux density distribution

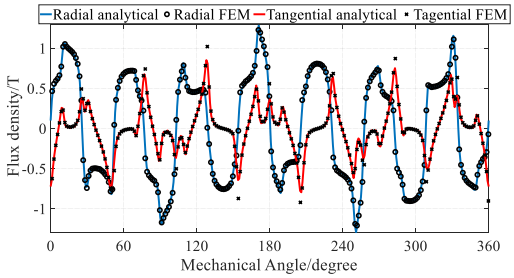

Fig. 5. Analytically predicted and FEM calculated results with on-load inner air-gap flux density distribution

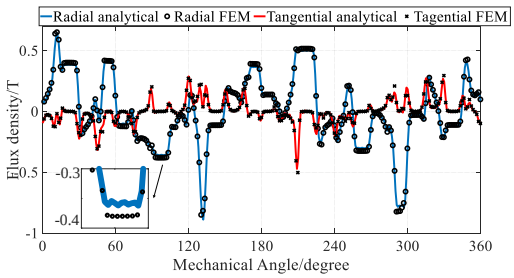

Fig. 6. Analytically predicted and FEM calculated results with on-load outer air-gap flux density distribution

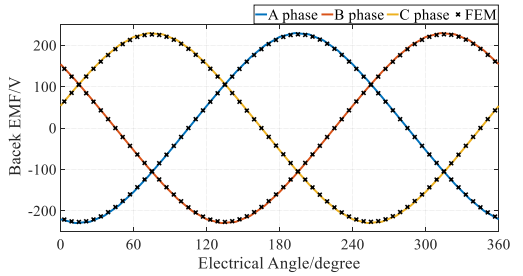

Fig. 7. Analytically predicted and FEM calculated results with three-phase back EMFs

4. Electromagnetic Performance Analysis

4.1. Equivalent d-q Axis Determination

When the MGDRM is electrified with three-phase AC currents, the magnetic field generated by stator windings interacts with that produced by PMs. So, the MGDRM can be regarded as a PMSM, when observed from the outer air-gap. However, the equivalent *d-q* axis of MGDRM is much more difficult to obtain compared with that of conventional PMSM, because the magnetic field distribution is changed by the modulation effect of ferromagnetic bars.

By adopting the subdomain model of MGDRM, the equivalent *d-q* axis of MGDRM can be gained. For the 14-pole MGDRM with nine ferromagnetic bars, the fundamental harmonic of windings is 2nd. Therefore, the radial-direction magnetic field distribution of 2nd harmonics on the middle of outer air gap can be obtained by substituting n=2 into (34):

$$B_{outer\_gap}(\bar{R},\theta) = G\sin(2\theta) + H\cos(2\theta) \tag{51}$$

$$with \quad \begin{cases} G = -A_2^{IV}\dfrac{R_4}{\bar{R}}\dfrac{P_2(\bar{R},R_5)}{E_2(R_4,R_5)} - B_2^{IV}\dfrac{R_5}{\bar{R}}\dfrac{P_2(\bar{R},R_4)}{E_2(R_5,R_4)} \\ H = C_2^{IV}\dfrac{R_4}{\bar{R}}\dfrac{P_2(\bar{R},R_5)}{E_2(R_4,R_5)} + D_2^{IV}\dfrac{R_5}{\bar{R}}\dfrac{P_2(\bar{R},R_4)}{E_2(R_5,R_4)} \end{cases} \tag{52}$$

where A_2^{IV}, B_2^{IV}, C_2^{IV}, D_2^{IV} are the second order Fourier coefficients of vector magnetic potential in (66), and $\bar{R}$ =(R_4+R_5)/2. Then, (51) can be further rewritten as:

$$B_{outer\_gap}(\bar{R},\theta) = \sqrt{G^2+H^2}\sin(2\theta+\vartheta) \tag{53}$$

with ϑ =arctan(H/G). So, the fundamental harmonic observed from stator windings is a sinusoidal wave with two pole pairs. If the *d-q* axis theory in traditional PMSM is applied to the MGDRM, the electrical angle of the equivalent *d* axis α on the outer air gap produced by PM can be calculated by:

$$\alpha = \begin{cases} \dfrac{\pi}{2} - \vartheta & \text{if } G>0 \\ -\dfrac{\pi}{2} - \vartheta & \text{if } G<0 \end{cases} \tag{54}$$

After obtaining the *d* axis angle for a certain modulator and rotor position, the variation rule among α, modulator and rotor position can be explored. Since the modulator pole structure has a period of $2\pi/Q$ and the inner rotor PMs has a period of $2\pi/P_i$ in circumferential direction, namely $A\big|_{\theta_i+2\pi/Q} = A\big|_{\theta_i}$ and $A_i\big|_{\varphi_i+2\pi/P_i} = A_i\big|_{\varphi_i}$, the *d* axis angular position is only calculated based on (54) with the range $\varphi_i \in [0, 2\pi/P_i]$, $\theta_i \in [0, 2\pi/Q]$. Fig. 8 shows the predicted *d* axis variation with φ_i and θ_i.

Figure 9 is the corresponding contour map of Fig. 8. To illustrate the relation among Ω_{in} Ω_{out} and the angular position of equivalent *d* axis, different rotating speed combinations are set as following: line 1 represents Ω_{in}= 900 r/min, Ω_{out}= 700 r/min; line 2 represents Ω_{in}= 600 r/min, Ω_{out}= 2000/3 r/min; line 3 represents Ω_{in}= 600 r/min, Ω_{out}= 200/3 r/min; line 4 represents Ω_{in}= -600 r/min, Ω_{out}= -2000/3 r/min. Figure 10 shows the comparison of the variation of the angular position of *d* axis by analytical method and FEM. For the analytical result, the gradient of the angular position of the *d* axis is a constant under four different conditions, and the value of that constant changes with different Ω_{in} and Ω_{out}. Actually, it can be generalized that the rotating speed of the *d* axis Ω_d satisfies [30]:

$$\Omega_d = P_i\Omega_{in} - Q\Omega_{out} \tag{55}$$

However, the *d* axis variation obtained by FEM does not strictly follow these lines, which is caused by magnetic saturation. The overall change rule of Ω_d by taking account of magnetic saturation still follows (55).

Hence, to produce a steady torque, the axis rotating magnetic field generated by the stator winding should keep relative still with the equivalent *d* axis. Hence, the frequency of stator winding should satisfy:

$$f = \Omega_d / 60 \tag{56}$$

Thus, the speed, torque and power relationship among the three rotating parts of MGDRM are similar to those of planetary gear.

Since the *d* axis can be calculated by using the angular position information of inner rotor and modulator in real time, i_d=0 control can be carried out for the MGDRM. Fig. 11 shows the output torque of inner rotor and modulator variation in one electrical period under i_d=0 control with D=5 A/mm^2, where T_{out} is set as the absolute value for a clear illustration. The torque difference becomes larger with the increase of RMS current density in the stator windings, that is to say, the magnetic saturation of the MGDRM becomes severe as the current in stator windings increases.

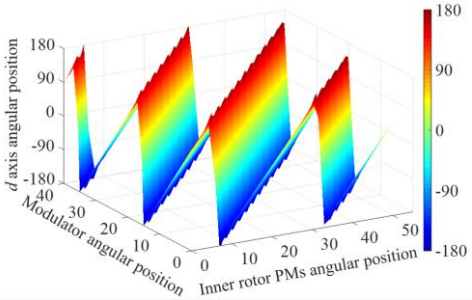

Fig. 8. *Variation of d axis with modulator angular position and inner rotor angular position*

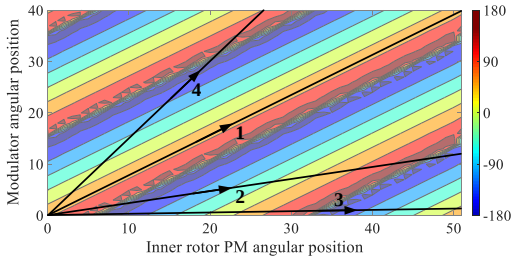

Fig. 9. *Gradient map of d axis variation with modulator angular position and inner rotor angular position*

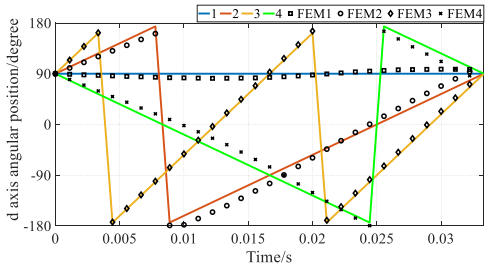

Fig. 10. *Analytically predicted and FEM calculated d axis variation under different rotating speeds*

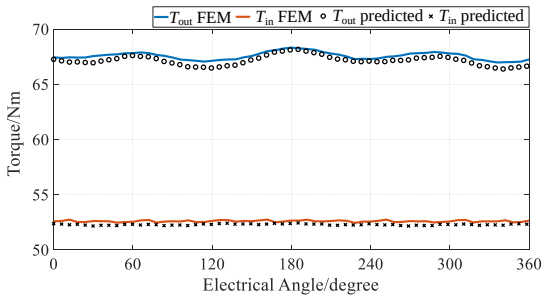

Fig. 11. *Analytically predicted and FEM calculated electromagnetic torques of inner rotor and modulator by adopting id=0 control*

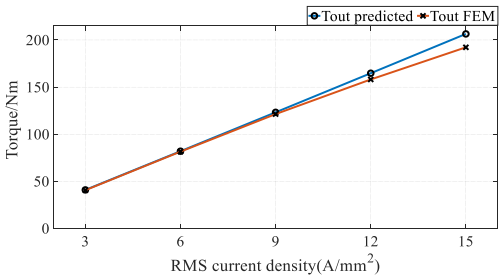

Fig. 12. *Analytically predicted and FEM calculated electromagnetic torque of outer rotor at different current densities*

4.2. d-q Axis Inductance Analysis and i_d=0 Control

The flux linkage in (49) can be divided into two parts, one is produced by the PMs, named as ψ_f ; another is produced by the stator windings. As for the later one, it can be written in an inductance form, so the flux linkage can be expressed as:

$$\begin{bmatrix}\psi_A(\theta)\\ \psi_B(\theta)\\ \psi_C(\theta)\end{bmatrix}=\begin{bmatrix}\psi_{fA}(\theta)\\ \psi_{fB}(\theta)\\ \psi_{fC}(\theta)\end{bmatrix}+\begin{bmatrix}L_{AA}(\theta) & M_{AB}(\theta) & M_{AC}(\theta)\\ M_{BA}(\theta) & L_{BB}(\theta) & M_{BC}(\theta)\\ M_{CA}(\theta) & M_{CB}(\theta) & L_{CC}(\theta)\end{bmatrix}\cdot\begin{bmatrix}i_A\\ i_B\\ i_C\end{bmatrix} \quad (57)$$

where θ is the angle between the axis of A phase and *d* axis. L_{ii} is the self inductance of phase *i*, M_{ij} is the mutual inductance between phase *i*, *j*. The self and mutual inductance can be obtained by only letting one phase be electrified and the remanence of PMs be zero. For instance, when the phase A is electrified with direct current I_A with an amplitude of 0.1 A, while I_B= I_C= 0, and B_r= 0. The flux linkage matrix $\boldsymbol{\psi}$ can be obtained via (49). Then, the self inductance and mutual inductance can be derived as:

$$L_{AA}=\frac{\psi_A}{I_A},\ M_{AB}=\frac{\psi_B}{I_A},\ M_{AC}=\frac{\psi_C}{I_A} \quad (58)$$

Figure 13 shows the comparison of L_{AA}, M_{AB} and M_{AC} by analytical model and FEM within an electric period. The saliency effect of MGDRMs is caused by the modulator, whose rotating speed is different from that of the equivalent *d* axis. So the rule that L_{AA} contains a second harmonic component with respect to electrical angle for conventional PMSMs is false for MGDRMs, as can be seen in Fig. 13. In addition, it can be obtained that the change of L_{AA} is only 0.93 percent due to the saliency effect of the modulator pieces, which means the air-gap permeance observed from stator can be regarded as a constant. Hence, the equivalent synchronous machine is a non-salient-pole one, namely L_d = L_q, where L_d, L_q are the *d*-axis and *q*-axis inductance, respectively. Hence, under i_d=0 control, the output torque of MGDRM can reach its maximum. Besides, L_d, L_q can be obtained by:

$$L_d=L_q=\frac{\psi_q}{I_q} \quad (59)$$

where ψ_q, I_q is the *q*-axis flux and *q*-axis current, respectively. They can be calculated by using Clark's Transformation and park's Transformation to find the projection of three-phase flux and current on the *q* axis [31], where the *q* axis is obtained by using the method in section IV part 1.

The values of L_d, L_q keep constant for a certain MGDRM with the condition on how Ω_{in} and Ω_{out} changing, which simplifies the control of MGDRM after *d*-*q* axis decoupling.

Under i_d=0 control, the phasor diagram can be plotted as Fig. 14, where the resistance stator winding is ignored. Thus, the power factor of MGDRM can be obtained by:

$$\cos(\varphi)=\frac{E_0}{\sqrt{E_0^2+(\omega L_q I_q)^2}} \tag{60}$$

where E_0 is the back EMF of one phase obtained from (50), ω is the angular speed of d axis, and $\omega=2\pi\Omega_d/60$.

The manufacture of double-rotor structure is a tough problem. The air-gap length directly influences the electromagnetic performance of MGDRM. Figure 15 shows the relation of outer rotor torque, q-axis inductance and power factor with the air gap length. It can be seen that the thicker the air-gap length is, the less the outer rotor torque will be. However, a very small air gap requires a high manufacture accuracy. Hence, it is a trade off between the electromagnetic performance and price. Besides, it can be seen from Fig. 15 that the power factor of the MGDRM is very low, that is a common drawback for flux-modulation electric machines due to the high self inductance and low PM flux linkage on the stator windings [23].

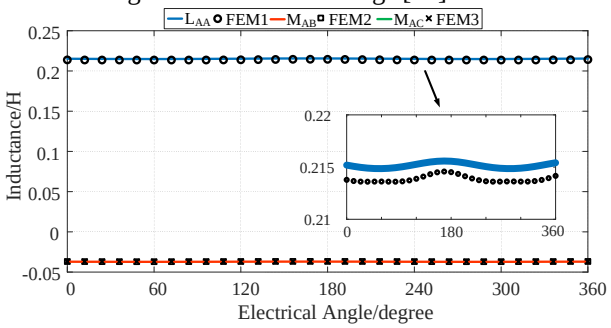

Fig. 13. *Self inductance and mutual inductance of one phase*

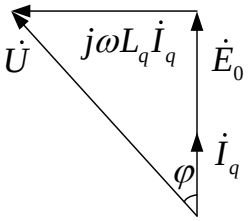

Fig. 14. *Phasor diagram when i_d= 0*

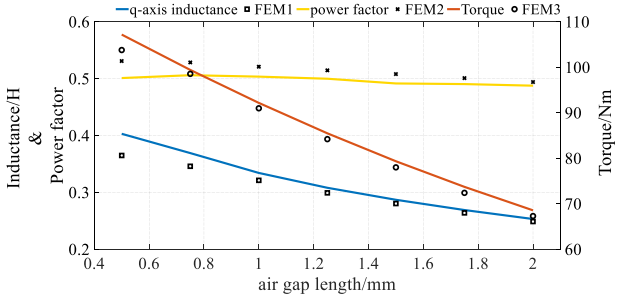

Fig. 15. *Variation of q-axis inductance, power factor and output torque with modulator thickness*

4.3. Demagnetization Capability Analysis

The permanent magnet suffers from the irreversible demagnetization under high-temperature working condition. It is assumed that the ambient temperature for the motors in EV to be 120 °C [32], and then the demagnetization risk of PMs at different current levels (in RMS value) are analyzed under i_d= 0 control. The PM material N35SHX is selected, and its remanence B'_r=1.08 T, while at the knee point, B_d=0.22 T. Thus, the absolute value of magnetic flux density distribution within PMs should be above B_d by considering different magnetization direction, otherwise irreversible demagnetization would happen. Since the outer surface of PMs is the closest to the armature windings, where the PMs have the highest risk of demagnetization, Fig. 16 shows the flux density distribution in the magnetization direction on the outer surface of PMs along the circumferential direction under different armature current. From Fig. 16, the flux density is below 0.22 T when the current density is 8 A/mm^2. Thus, the maximum safe operation current density of MGDRM is 7 A/mm^2 at 120 °C. Also, a comparison between the analytical prediction and FEM where D= 5 A/mm^2, temperature is 20 °C and D= 7 A/mm^2, temperature is 120 °C is shown in Fig. 17-18. It can be observed that the larger the armature current and the higher the temperature are, the smaller of minimum flux density on some places of outer surface of PMs is. Thus, the demagnetization risk goes higher with the increase of armature current and temperature. Besides, a good agreement can be seen between the analytical prediction and FEM.

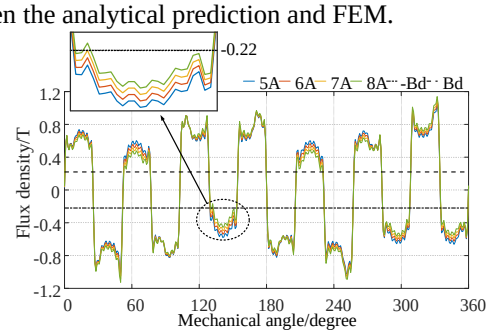

Fig. 16. *Analytically predicted flux density distribution in the magnetization direction on the surface of PMs at 120 °C at different current levels*

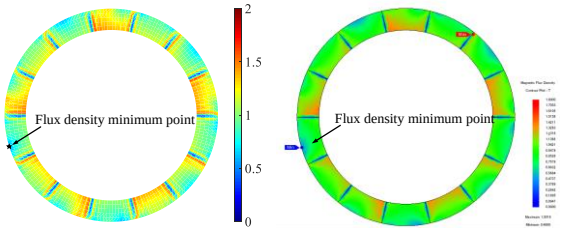

(a) *(b)*

Fig. 17. *Flux density distribution of PMs with D= 5 A, temperature of 20 °C (a) Analytical prediction, (b) FEM result.*

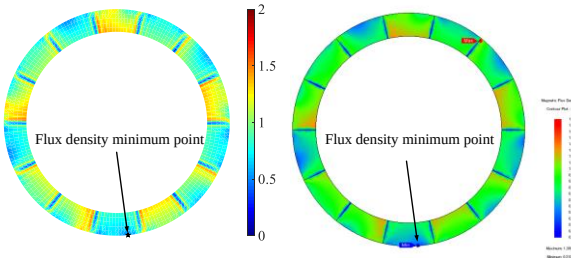

(a) *(b)*

Fig. 18. *Flux density distribution of PMs with D= 7 A, temperature of 120 °C (a) Analytical prediction, (b) FEM result.*

5. Conclusion

In this paper, a subdomain model is developed for predicting the magnetic field distribution and electromagnetic performances of MGDRMs. The analytical model can give the accurate results with a significant time saving, when it is compared with the FEM. Moreover, based on the proposed model, the equivalent *d-q* axis is derived. And the MGDRM is proved to be a non-salient-pole synchronous machine, where the *id*=0 control can be exerted, and maximal output torque is obtained. Furthermore, the power factor and the demagnetization capability under *id*=0 control are analysed. Finally, the analytical model is validated by using the FEM. It tells that this model can be a useful tool for the primary stage design and optimization of MGDRMs.

Acknowledgement

This work was supported in part by a grant (Project No. 51677159) from the Natural Science Foundation of China (NSFC), China. Also, the work was supported by a grant (Project No. JCYJ20180307123918658) from the Science Technology and Innovation Committee of Shenzhen Municipality, Shenzhen, China. Moreover, it was supported in part by a grant (Project No. CityU 21201216) from the Research Grants Council of HKSAR, China.

References

[1] Emadi, A., Young Joo, L., and Rajashekara, K., 'Power Electronics and Motor Drives in Electric, Hybrid Electric, and Plug-in Hybrid Electric Vehicles', *IEEE Transactions on Industrial Electronics*, 2008, 55, (6), pp. 2237-2245.

[2] Mashadi, B. and Emadi, S.A., 'Dual-Mode Power-Split Transmission for Hybrid Electric Vehicles', *IEEE Trans. Veh. Technol.*, 2010, 59, (7), pp. 3223-3232.

[3] Liu, C., 'Emerging Electric Machines and Drives — an Overview', *IEEE Trans. Energy Convers.*, 2018, 33, (4), pp. 2270-2280.

[4] Zhao, H., Liu, C., Song, Z., and Yu, J., 'Analytical Modeling and Comparison of Two Consequent-Pole Magnetic-Geared Machines for Hybrid Electric Vehicles', *Energies*, 2019, 12, (10).

[5] Bai, J., Liu, J., Zheng, P., and Tong, C., 'Design and Analysis of a Magnetic-Field Modulated Brushless Double-Rotor Machine—Part I: Pole Pair Combination of Stator, Pm Rotor and Magnetic Blocks', *IEEE Transactions on Industrial Electronics*, 2019, 66, (4), pp. 2540-2549.

[6] Sun, L., Cheng, M., and Jia, H., 'Analysis of a Novel Magnetic-Geared Dual-Rotor Motor with Complementary Structure', *IEEE Transactions on Industrial Electronics*, 2015, 62, (11), pp. 6737-6747.

[7] Liu, C. and Chau, K.T., 'Electromagnetic Design of a New Electrically Controlled Magnetic Variable-Speed Gearing Machine', *Energies*, 2014, 7, (3), pp. 1539-1554.

[8] Zhao, H. and Liu, C., Design of an Effective Double-Rotor Machine with Robust Mechanical Structure', (Asia-Pacific Magnetic Recording Conference 2018, 2018)

[9] Wang, Y., Niu, S., and Fu, W., 'Electrical-Continuously Variable Transmission System Based on Doubly Fed Flux-Bidirectional Modulation', *IEEE Transactions on Industrial Electronics*, 2017, 64, (4), pp. 2722-2731.

[10] Ren, X., Li, D., Qu, R., and Zou, T., 'A Brushless Dual-Mechanical-Port Dual-Electrical-Port Machine with Spoke Array Magnets in Flux Modulator', *IEEE Trans. Magn.*, 2017, 53, (11), pp. 1-6.

[11] Atallah, K., Calverley, S., and Howe, D., 'Design, Analysis and Realisation of a High-Performance Magnetic Gear', *IEE Proceedings-Electric Power Applications*, 2004, 151, (2), pp. 135-143.

[12] Severson, E., Nilssen, R., Undeland, T., and Mohan, N., 'Magnetic Equivalent Circuit Modeling of the Ac Homopolar Machine for Flywheel Energy Storage', *IEEE Trans. Energy Convers.*, 2015, 30, (4), pp. 1670-1678.

[13] Amrhein, M. and Krein, P.T., '3-D Magnetic Equivalent Circuit Framework for Modeling Electromechanical Devices', *IEEE Trans. Energy Convers.*, 2009, 24, (2), pp. 397-405.

[14] Bash, M.L., Williams, J.M., and Pekarek, S.D., 'Incorporating Motion in Mesh-Based Magnetic Equivalent Circuits', *IEEE Trans. Energy Convers.*, 2010, 25, (2), pp. 329-338.

[15] O'Connell, T.C. and Krein, P.T., 'A Schwarz–Christoffel-Based Analytical Method for Electric Machine Field Analysis', *IEEE Trans. Energy Convers.*, 2009, 24, (3), pp. 565-577.

[16] Boughrara, K., Zarko, D., Ibtiouen, R., Touhami, O., and Rezzoug, A., 'Magnetic Field Analysis of Inset and Surface-Mounted Permanent-Magnet Synchronous Motors Using Schwarz–Christoffel Transformation', *IEEE Trans. Magn.*, 2009, 45, (8), pp. 3166-3178.

[17] Jalali, P., Boroujeni, S.T., and Bianchi, N., 'Analytical Modeling of Slotless Eccentric Surface-Mounted Pm Machines Using a Conformal Transformation', *IEEE Trans. Energy Convers.*, 2016, 32, (2), pp. 658-666.

[18] Zhu, Z.Q., Howe, D., Bolte, E., and Ackermann, B., 'Instantaneous Magnetic Field Distribution in Brushless Permanent Magnet Dc Motors. I. Open-Circuit Field', *IEEE Trans. Magn.*, 1993, 29, (1), pp. 124-135.

[19] Gysen, B., Meessen, K., Paulides, J., and Lomonova, E., 'General Formulation of the Electromagnetic Field Distribution in Machines and Devices Using Fourier Analysis', *IEEE Trans. Magn.*, 2009, 46, (1), pp. 39-52.

[20] Rahideh, A., Vahaj, A.A., Mardaneh, M., and Lubin, T., 'Two-Dimensional Analytical Investigation of the Parameters and the Effects of Magnetisation Patterns on the Performance of Coaxial Magnetic Gears', IET Electrical Systems in Transportation, 2017, 7, (3), pp. 230-245..

[21] Zhu, Z.Q., Wu, L.J., and Xia, Z.P., 'An Accurate Subdomain Model for Magnetic Field Computation in Slotted Surface-Mounted Permanent-Magnet Machines', *IEEE Trans. Magn.*, 2010, 46, (4), pp. 1100-1115.

[22] Boughrara, K., Lubin, T., and Ibtiouen, R., 'General Subdomain Model for Predicting Magnetic Field in Internal and External Rotor Multiphase Flux-Switching Machines Topologies', *IEEE Trans. Magn.*, 2013, 49, (10), pp. 5310-5325.

[23] Oner, Y., Zhu, Z.Q., Wu, L.J., Ge, X., Zhan, H., and Chen, J.T., 'Analytical on-Load Subdomain Field Model of Permanent-Magnet Vernier Machines', *IEEE Transactions on Industrial Electronics*, 2016, 63, (7), pp. 4105-4117.

[24] Lubin, T., Mezani, S., and Rezzoug, A., '2-D Exact Analytical Model for Surface-Mounted Permanent-Magnet Motors with Semi-Closed Slots', *IEEE Trans. Magn.*, 2011, 47, (2), pp. 479-492.

[25] Shakibapour, F., Rahideh, A., and Mardaneh, M., '2d Analytical Model for Heteropolar Active Magnetic Bearings Considering Eccentricity', *IET Electr. Power Appl.*, 2018, 12, (5), pp. 614-626.

[26] Zhang, X., Liu, X., Liu, J., and Chen, Z., 'Analytical Investigation on the Power Factor of a Flux-Modulated Permanent-Magnet Synchronous Machine', *IEEE Trans. Magn.*, 2015, 51, (11), pp. 1-4.

[27] Sun, L., Cheng, M., Zhang, J.W., and Song, L.H., 'Analysis and Control of Complementary Magnetic-Geared Dual-Rotor Motor', *IEEE Transactions on Industrial Electronics*, 2016, 63, (11), pp. 6715-6725.

[28] Lubin, T., Mezani, S., and Rezzoug, A., 'Analytical Computation of the Magnetic Field Distribution in a Magnetic Gear', *IEEE Trans. Magn.*, 2010, 46, (7), pp. 2611-2621.

[29] Farlow, S.J., *Partial Differential Equations for Scientists and Engineers*, (Courier Corporation, 1993)

[30] Bai, J.G., Zheng, P., Tong, C.D., Song, Z.Y., and Zhao, Q.B., 'Characteristic Analysis and Verification of the Magnetic-Field-Modulated Brushless Double-Rotor Machine', *IEEE Transactions on Industrial Electronics*, 2015, 62, (7), pp. 4023-4033.

[31] Jahns, T.M., 'Flux-Weakening Regime Operation of an Interior Permanent-Magnet Synchronous Motor Drive', *IEEE Trans. Ind. Appl.*, 1987, (4), pp. 681-689.

[32] Pellegrino, G., Vagati, A., Boazzo, B., and Guglielmi, P., 'Comparison of Induction and Pm Synchronous Motor Drives for Ev Application Including Design Examples', *IEEE Trans. Ind. Appl.*, 2012, 48, (6), pp. 2322-2332.

Appendix

Table 4 shows the expressions of the Fourier coefficients of each subdomains when boundary conditions are applied.

Table 4 Fourier Coefficients Applied to Boundary Conditions

Regions	Fourier coefficient	
I	$A_n^I = \frac{1}{\pi}\int_0^{2\pi} A_{II}(R_2,\theta)\cos(n\theta)d\theta\,,\ C_n^I = \frac{1}{\pi}\int_0^{2\pi} A_{II}(R_2,\theta)\sin(n\theta)d\theta$	(61)
	$X_n(r) = \frac{E_n(R_2,r)}{P_n(R_2,R_1)}\cdot\frac{f_n'(R_1)}{n} - \frac{P_n(r,R_1)}{P_n(R_2,R_1)} f_n(R_2) + f_n(r)\,,\ f_n(r) = \begin{cases} \frac{4B_r r p_{in}}{\pi(1-n^2)} & \text{if } n = kp_i \text{ with } k=1,3,5,... \\ \frac{2B_r}{\pi} r\ln r & \text{if } n = p_i = 1 \end{cases}$	(62)
II	$A_n^{II} = \frac{1}{\pi}\int_0^{2\pi} \left.\frac{\partial A_{II}}{\partial r}\right\|_{r=R_2} \cos(n\theta)d\theta\,,\ C_n^{II} = \frac{1}{\pi}\int_0^{2\pi} \left.\frac{\partial A_{II}}{\partial r}\right\|_{r=R_2} \sin(n\theta)d\theta\,,$	
	$B_n^{II} = \frac{1}{\pi}\int_0^{2\pi} f(\theta)\cos(n\theta)d\theta\,,\ D_n^{II} = \frac{1}{\pi}\int_0^{2\pi} f(\theta)\sin(n\theta)d\theta$	(63)
III	$A_k^i = \frac{2}{\beta}\int_{\theta_i}^{\theta_i+\beta} A_{II}(R_3,\theta)\cos(\frac{k\pi}{\beta}(\theta-\theta_i))d\theta\,,\ B_k^i = \frac{2}{\beta}\int_{\theta_i}^{\theta_i+\beta} A_{III}(R_4,\theta)\cos(\frac{k\pi}{\beta}(\theta-\theta_i))d\theta$	(64)
	$A_0^i + B_0^i\ln R_3 = \frac{1}{\beta}\int_{\theta_i}^{\theta_i+\beta} A_{II}(R_3,\theta)d\theta\,,\ A_0^i + B_0^i\ln R_4 = \frac{1}{\beta}\int_{\theta_i}^{\theta_i+\beta} A_{IV}(R_4,\theta)d\theta$	(65)
IV	$A_n^{IV} = \frac{1}{\pi}\int_0^{2\pi} g(\theta)\cos(n\theta)d\theta\,,\ C_n^{IV} = \frac{1}{\pi}\int_0^{2\pi} g(\theta)\sin(n\theta)d\theta\,,$	
	$B_n^{IV} = \frac{1}{\pi}\int_0^{2\pi} h(\theta)\cos(n\theta)d\theta\,,\ D_n^{IV} = \frac{1}{\pi}\int_0^{2\pi} h(\theta)\sin(n\theta)d\theta$	(66)
V	$A_t^j = \frac{2}{\delta}\int_{\theta_j}^{\theta_j+\delta} A_{IV}(R_5,\theta)\cos(\frac{t\pi}{\delta}(\theta-\theta_j))d\theta\,,\ B_t^j = \frac{2}{\delta}\int_{\theta_j}^{\theta_j+\delta} A_l(R_6,\theta)\cos(\frac{t\pi}{\delta}(\theta-\theta_j))d\theta\ \ (l=j)$	(67)
	$A_0^j + B_0^j\ln R_5 = \frac{1}{\delta}\int_{\theta_j}^{\theta_j+\delta} A_{IV}(R_5,\theta)d\theta\,,\ A_0^j + B_0^j\ln R_6 = \frac{1}{\delta}\int_{\theta_j}^{\theta_j+\delta} A_l(R_6,\theta)d\theta\ \ (l=j)\,,\quad B_0^j = \frac{\gamma}{\delta}\cdot\frac{1}{2}\mu_0 J_l(R_7^2 - R_6^2)$	(68)
VI	$A_m^l = \frac{2}{\gamma}\int_{\theta_j}^{\theta_j+\delta} \left.\frac{\partial A_j}{\partial r}\right\|_{r=R_6} \cos(\frac{m\pi}{\gamma}(\theta-\theta_j-\frac{1}{2}(\delta-\gamma)))d\theta$	(69)